Article

A gated quantum dot strongly coupled to an optical microcavity

Daniel Najer[1]*, Immo Söllner[1], Pavel Sekatski[1], Vincent Dolique[2], Matthias C. Löbl[1], Daniel Riedel[1], Rüdiger Schott[3], Sebastian Starosielec[1], Sascha R. Valentin[3], Andreas D. Wieck[3], Nicolas Sangouard[1], Arne Ludwig[3] & Richard J. Warburton[1]

The strong-coupling regime of cavity quantum electrodynamics (QED) represents the light–matter interaction at the fully quantum level. Adding a single photon shifts the resonance frequencies—a profound nonlinearity. Cavity QED is a test bed for quantum optics[1-3] and the basis of photon–photon and atom–atom entangling gates[4,5]. At microwave frequencies, cavity QED has had a transformative effect[6], enabling qubit readout and qubit couplings in superconducting circuits. At optical frequencies, the gates are potentially much faster; the photons can propagate over long distances and can be easily detected. Following pioneering work on single atoms[1-3,7], solid-state implementations using semiconductor quantum dots are emerging[8-15]. However, miniaturizing semiconductor cavities without introducing charge noise and scattering losses remains a challenge. Here we present a gated, ultralow-loss, frequency-tunable microcavity device. The gates allow both the quantum dot charge and its resonance frequency to be controlled electrically. Furthermore, cavity feeding[10,11,13-17], the observation of the bare-cavity mode even at the quantum dot–cavity resonance, is eliminated. Even inside the microcavity, the quantum dot has a linewidth close to the radiative limit. In addition to a very pronounced avoided crossing in the spectral domain, we observe a clear coherent exchange of a single energy quantum between the 'atom' (the quantum dot) and the cavity in the time domain (vacuum Rabi oscillations), whereas decoherence arises mainly via the atom and photon loss channels. This coherence is exploited to probe the transitions between the singly and doubly excited photon–atom system using photon-statistics spectroscopy[18]. The work establishes a route to the development of semiconductor-based quantum photonics, such as single-photon sources and photon–photon gates.

A resonant, low-loss, low-volume cavity boosts greatly the light–matter interaction so that cavity QED can potentially provide a highly coherent interface between single photons and single atoms. The metric for the coherence is the cooperativity C, the ratio of the coherent coupling squared to the loss rates, $C = 2g^2/(\kappa\gamma)$ (g is the coherent photon–atom coupling, κ is the cavity loss rate and γ is the decay rate of the atom into non-cavity modes). The potential for achieving a high cooperativity gives cavity QED a central role in the development of high-fidelity quantum gates.

In the microwave domain, a transmon 'atom' exhibits strong coupling to a cavity photon[6], facilitating remote transmon–transmon coupling via a virtual photon. Recently, the transmon was replaced with a semiconductor quantum dot (QD), and coupling was observed between a microwave photon and both charge[19] and spin qubits[20-22]. In contrast to microwave photons, optical-frequency photons can carry quantum information over very large distances and therefore play an indispensable role in quantum communication. Creating an optical photon–photon gate depends critically on a high-cooperativity

photon–atom interface and on efficient photonic engineering[5]. Cavity QED can potentially achieve both simultaneously. Translating these concepts to the solid state is important for developing on-chip quantum technology. The most promising solid-state 'atom' is a self-assembled semiconductor QD: an InGaAs QD in a GaAs host is a bright and fast emitter of highly indistinguishable photons[23,24], and a QD spin provides the resource required for atom–photon and photon–photon gates. However, a low-noise, high-cooperativity and high-efficiency interface between a single photon and a single QD does not yet exist.

In QD cavity QED, one key problem is the almost ubiquitous observation of scattering from the bare cavity even at the QD–cavity resonance[10,11,13-17]. This 'cavity feeding' is the manifestation of complex noise processes in the semiconductor host[11]. Another key problem is the trade-off between the coupling g and the loss rates κ and γ in monolithic devices, for instance, in micropillar[8,23] or photonic-crystal cavities[9-11,13-15]: as such devices are made smaller, in an attempt to boost g, both κ and γ tend to increase. The increase in κ, reflecting a deterioration in the quality factor (Q) of the microcavity, arises on account
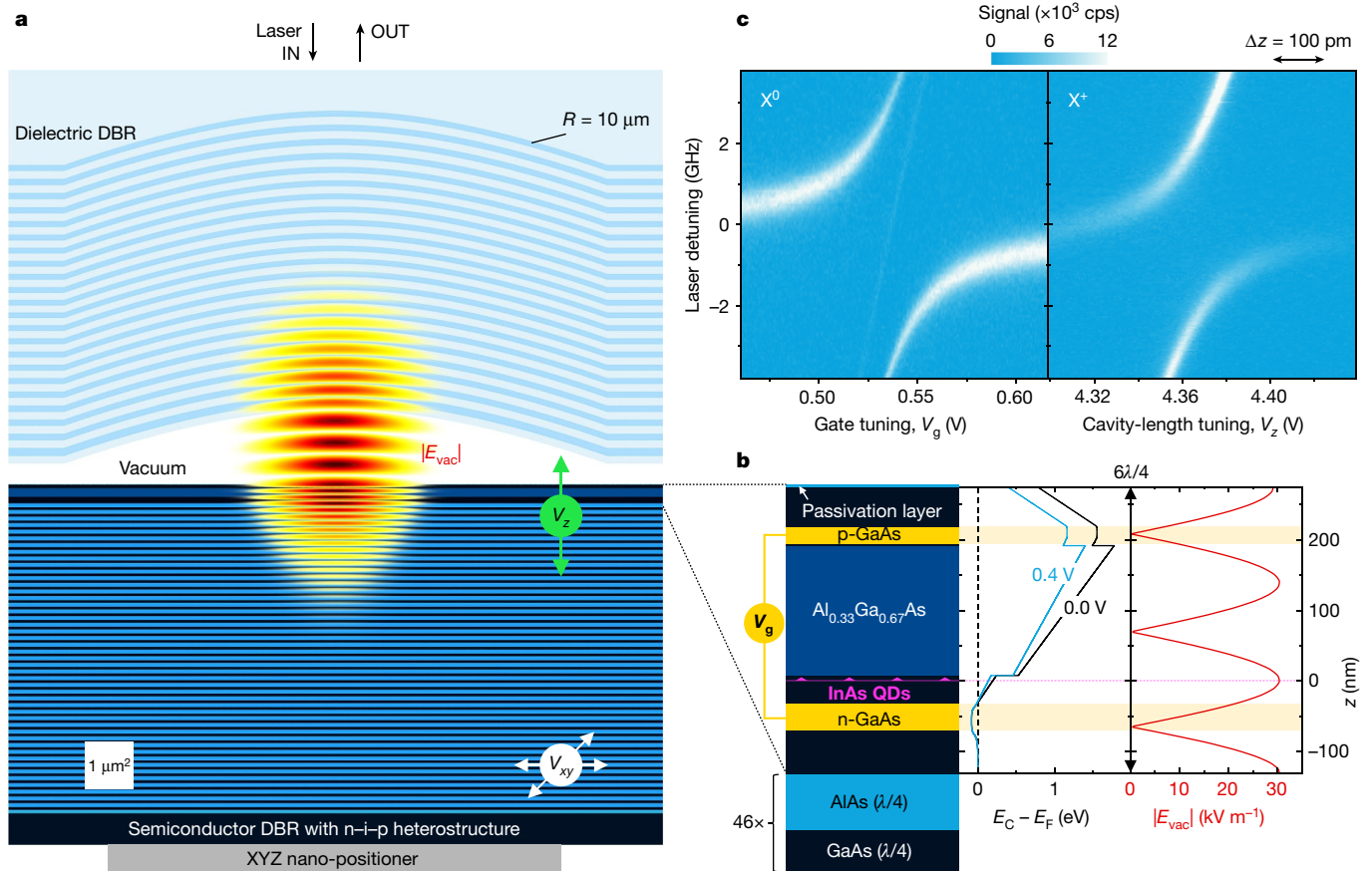
Fig. 1 | Gated QD in a tunable microcavity: design and realization.
a, Simulation of the vacuum electric field $|E_{vac}|$ in the microcavity (image to scale). The bottom mirror is a distributed Bragg reflector (DBR) consisting of 46 pairs of AlAs (thickness $\lambda/4$) and GaAs ($\lambda/4$). (λ is the wavelength in each material.) The top mirror is fabricated in a silica substrate. It has a radius of curvature of $R = 10$ μm and consists of 22 pairs of silica ($\lambda/4$) and tantala ($\lambda/4$). The layer of QDs is located at the vacuum field anti-node, one wavelength beneath the surface. The vacuum gap has a height of $3\lambda/2$. The voltage V_{xy} (V_z) controls the lateral (vertical) position of the QD with respect to the fixed top mirror. **b**, The top part of the semiconductor heterostructure. A voltage V_g is applied across the n–i–p diode. V_g controls the QD charge via Coulomb blockade and within a Coulomb blockade plateau the exact QD optical

frequency via the d.c. Stark effect. Free-carrier absorption in the p layer[28] is minimized by positioning it at a node of the vacuum field. A passivation layer suppresses surface-related absorption[25]. E_C, conduction band edge; E_F, Fermi energy. **c**, Laser detuning (Δ_L) versus cavity detuning (Δ_C) of a neutral QD exciton (X^0) and a positively charged exciton (X^+) in the same QD. Cavity detuning is achieved by tuning the QD at a fixed microcavity frequency (X^0) and by tuning the microcavity frequency at a fixed QD frequency (X^+). For X^0, the weak signal close to the bare-exciton frequency arises from weak coupling to the other orthogonally polarized X^0 transition and is unrelated to cavity feeding (see Extended Data Fig. 3a, b). Data in **c** are from QD1 (see Fig. 2) at a magnetic field of $B = 0.00$ T.

of increased scattering and absorption; the increase in γ reflects an inhomogeneous broadening in the emitter frequency. The increase in the loss rates is only partly a consequence of fabrication imperfections. An additional factor is the GaAs surface, which pins the Fermi energy mid-gap, resulting in surface-related absorption[25] and charge noise.

Here, the QD exhibits close-to-transform-limited linewidths even in the microcavity; the microcavity has an ultrahigh Q factor but small mode volume. Both the frequency and lateral position of the cavity can be tuned in situ via a nano-positioner (Fig. 1a). The QD exciton is far in the strong-coupling regime of cavity QED ($g \gg \kappa, g \gg \gamma$). Strong coupling is achieved on both neutral and charged excitons in the same QD by tuning both the QD charge and the microcavity frequency in situ. The output is close to a simple Gaussian beam. We achieve a cooperativity of $C = 150$, crucially eliminating cavity feeding, and find other sources of noise to be very weak. Equivalently, the β factor, the probability of the excited atom emitting into the cavity mode, is as high as 99.7%. The coherence of the coupled QD–cavity system is demonstrated most clearly by the observation of a very clear atom–photon exchange in the time domain (a vacuum Rabi oscillation).

The design of the QD microcavity is guided by three principles. First and foremost, a self-assembled QD benefits enormously from electrical

control via the conducting gates of a diode structure. A gated QD in high-quality material gives close-to-transform-limited linewidths[26], control over both the optical frequency via the Stark effect and the QD charge state via Coulomb blockade[27]. We therefore include electrical gates in the cavity device. This is non-trivial: the gates themselves, n-doped and p-doped regions in the semiconductor, absorb light via free-carrier absorption, and they are not obviously compatible with a high-Q cavity. Also, the gates inevitably create electric fields in the device, resulting in absorption via the Franz–Keldysh mechanism. Second, in order to achieve narrow QD linewidths in the cavity, we minimize the area of the free GaAs surface to reduce surface-related noise. Finally, we include a mechanism for in situ tuning of the cavity, both in frequency and in lateral position, to allow a full exploration of the parameter space.

We employ a miniaturized Fabry–Pérot cavity consisting of a semiconductor heterostructure and external top mirror (Fig. 1a). The heterostructure has an n–i–p design with the QDs in the intrinsic (i) region (Fig. 1b and Methods). The QDs are located at an antinode of the vacuum field; the p layer is located at the node of the photon field to minimize free-carrier absorption[28] (Fig. 1b). Mobile electrons absorb considerably less than mobile holes[28], so that it is not imperative to place the n
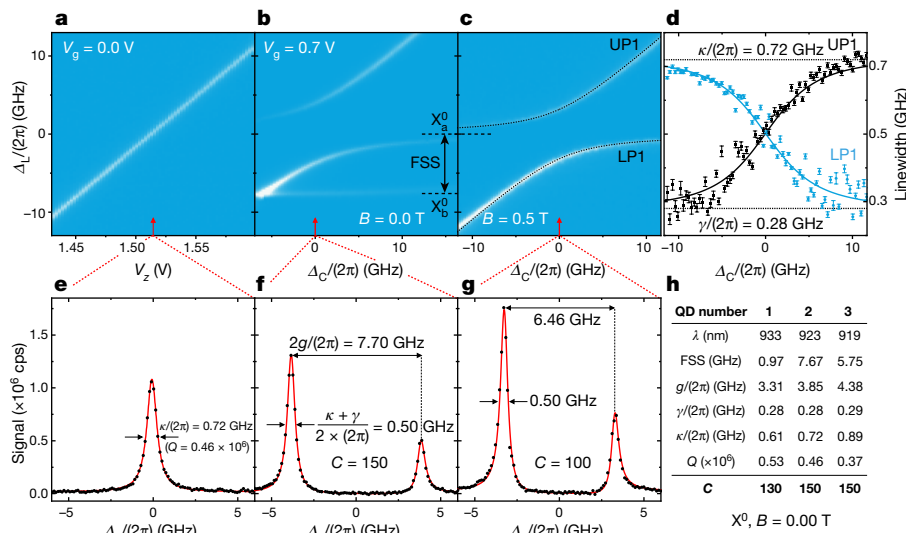
Fig. 2 | Strong coupling of a QD exciton in the microcavity. Spectra recorded by measuring the photons scattered by the microcavity–QD system at a temperature of 4.2 K, rejecting the reflected laser light with a polarization-based dark-field technique[26,29]. Data shown were taken on the X^0 transition. **a, e**, Signal measured with the QD far-detuned from the microcavity to determine the photon loss rate κ (equivalently, the quality factor Q). **b, f**, X^0 at a magnetic field of $B = 0.00$ T, showing strong coupling to one FSS transition and weak coupling to the other (there is an almost perfect alignment of the X^0 and microcavity axes). From the spectra, we determine g, κ, γ and C (as defined in the main text). **c, d, g**, X^0 at $B = 0.50$ T: the magnetic field increases the FSS. C is smaller than at $B = 0.00$ T because the X^0 transitions become circularly polarized and couple less strongly to the linearly polarized microcavity mode. The simple avoided crossing in **c** enables the determination of κ and γ by using data at all values of Δ_C. The dotted lines in **c** and solid lines in **d–g** are fits to a solution of the Jaynes–Cummings Hamiltonian in the limit of very small average photon occupation[17]. **h**, Summary of strong-coupling parameters recorded for X^0 at $B = 0.00$ T on three separate QDs using the same microcavity mode. In all three cases, $C > 100$. Error bars in **d** are one standard error. Data in **a–g** are from X^0 in QD2.

doping at a node of the vacuum field. The n layer begins 25 nm 'below' the QDs, so that they are in tunnel-contact with the Fermi sea in the n layer; that is, the QDs are in the Coulomb blockade regime. The bottom mirror is a semiconductor distributed Bragg reflector (DBR) and the top mirror consists of a 10-μm-radius dielectric DBR (see Methods). The position of the contacted sample is controlled in situ with respect to the top mirror. We find that surface-related absorption limits the Q factor to 2.0×10^4. This represented a major problem in the development of this device; to solve it, the GaAs surface was passivated by replacing the native oxide with a few-nanometre-thick alumina layer[25]. With surface passivation, the fully contacted device had a Q factor close to 10^6. The mode volume is $1.4\lambda_0^3$ (where λ_0 is the free-space wavelength).

We excite the QD–microcavity system with a resonant laser (continuous-wave), initially with an average photon occupation much less than one ($\langle n \rangle \approx 0.05$), and detect the scattered photons[26,29]. The fundamental microcavity mode splits into two linearly polarized modes, separated by 32 GHz, predominantly on account of a weak birefringence in the semiconductor. The neutral exciton also splits into a linearly polarized doublet, X_a^0 and X_b^0, via fine-structure splitting (FSS). QDs are chosen so that the microcavity and X^0 axes are closely aligned. The FSS varies among QDs and can be small enough so that both X_a^0 and X_b^0 couple to the same microcavity mode. In such cases (for example, QD1 in Fig. 2h), this complication can be avoided by applying a magnetic field that pushes X_a^0 and X_b^0 apart via the Zeeman effect. Alternatively, the charged exciton X^+, which has just one optical resonance at zero magnetic field, can be probed.

When the microcavity and QD optical frequency come into resonance, we observe a clear avoided crossing in the spectral response (Fig. 1c), signifying strong coupling. We achieve strong coupling on different charge states in the same QD (Fig. 1c), also on many different QDs (Fig. 2h and Methods). The cavity–emitter detuning is controlled by tuning either the QD (voltage V_g) or the microcavity (voltage V_z).
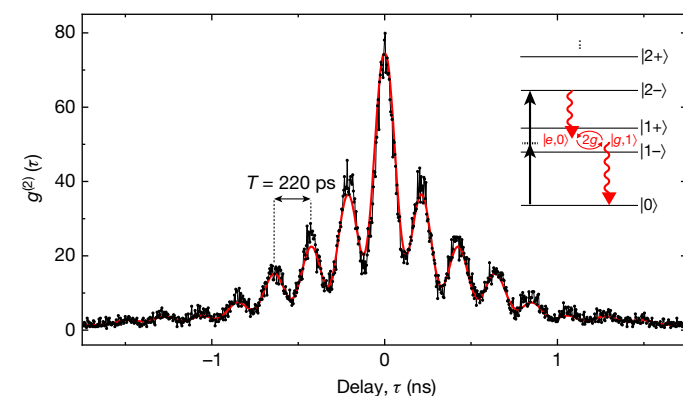
At the QD–cavity resonance, mixed states—the polaritons—form. Between the lower and upper polaritons (LP1 and UP1, respectively),

there is no trace of the bare-microcavity mode (Fig. 2f, g). These results demonstrate that cavity feeding has been eliminated, as a consequence of the electrical control via the gates. Coulomb blockade ensures that the QD is always in the charge state that couples to the microcavity mode. (A change of charge detunes the QD, leading to scattering from the bare-microcavity mode.) Phonon-assisted excitation of off-resonant QDs is clearly negligible.

A full spectral analysis determines the parameters g, κ and γ (Fig. 2), giving $\gamma/(2\pi) = 0.28$ GHz (Fig. 2). The transform limit for these QDs is 0.30 ± 0.05 GHz, where the uncertainty accounts for QD-to-QD fluctuations (see Methods). The measured $\gamma/(2\pi)$, 0.28 GHz, corresponds to the ideal limit to within the uncertainties of 10%–20%. The linewidths

Fig. 3 | Time-resolved vacuum Rabi oscillations. Intensity autocorrelation function $g^{(2)}(\tau)$ as a function of delay τ for $\Delta_C = 0.73g$ (detuned via cavity length) and $\Delta_L = -0.13g$. The inset shows the first few rungs of the Jaynes–Cummings ladder. The laser drives the two-photon transition $|0\rangle \leftrightarrow |2-\rangle$. The solid red line is the result of calculating $g^{(2)}(\tau)$ from the Jaynes–Cummings Hamiltonian using g, κ and γ from the spectroscopy experiments (Fig. 2) and Rabi coupling $\Omega/(2\pi) = 0.16$ GHz. Data are from X^0 in QD1 at $B = 0.40$ T. $|e\rangle$, excited state; $|g\rangle$, ground state.
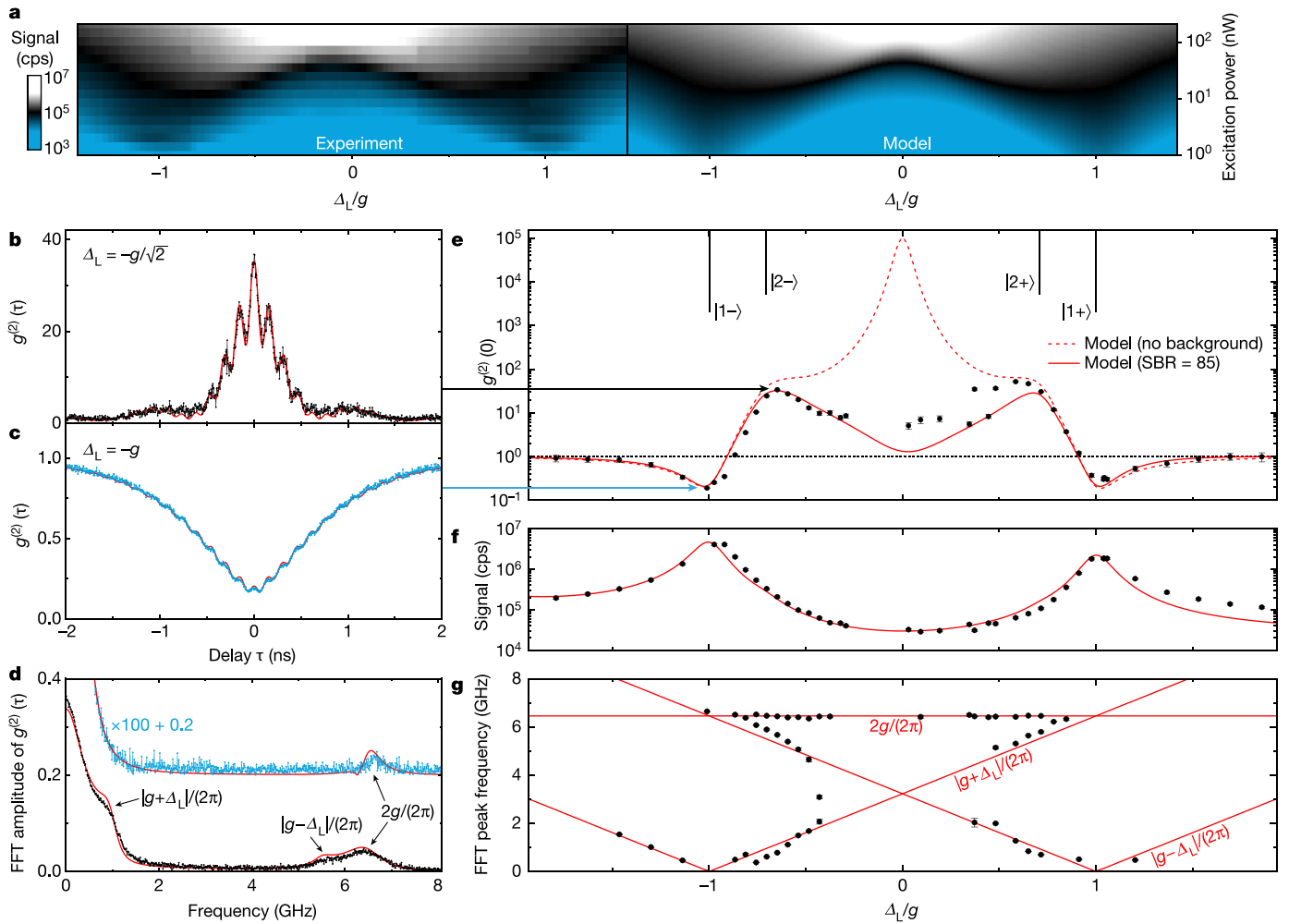
Fig. 4 | Strong coupling versus driving frequency and power. a, Signal versus Δ_L for $\Delta_C = 0$. At low power, LP1 and UP1 are clearly observed. As the power increases, the higher rungs of the Jaynes–Cummings ladder are populated. **b**, $g^{(2)}(\tau)$ for $\Delta_C = 0$ and $\Delta_L = -g/\sqrt{2}$. **c**, $g^{(2)}(\tau)$ for $\Delta_C = 0$ and $\Delta_L = -g$. **d**, Fast Fourier transform (FFT) of $g^{(2)}(\tau)$ in **b** and **c**. **e–g**, $g^{(2)}(0)$, signal and FFT peak frequency of $g^{(2)}(\tau)$ versus Δ_L for $\Delta_C = 0$. The solid red lines in **b–g** ('model' in **a**) result from a calculation of $g^{(2)}(\tau)$ (signal) from the Jaynes–Cummings Hamiltonian using g, κ

and γ from the spectroscopy experiments (Fig. 2). The Rabi coupling is $\Omega/(2\pi) = 0.14$–1.90 GHz (**a**) and 0.07–0.11 GHz (**b–g**) and a signal-to-background ratio of SBR = 20 (**a**) and 85 (**b–g**) was included. In **e**, the dashed red line shows the theoretical limit without the laser background. Error bars in **e–g** are one standard error. Data in **a** are from X$^+$ in QD1 at $B = 0.00$ T; data in **b–g** are from X^0 in QD2 at $B = 0.50$ T.

---

in the microcavity match the best QD linewidths reported so far[26]. The coupling g lies in the gigahertz regime, pointing to potentially very fast quantum operations. g corresponds closely to that expected considering the geometry of the device (Fig. 1b) and the QD optical dipole. For QD2 at zero magnetic field, $g/\gamma = 14$ and $g/\kappa = 5.3$, corresponding to a cooperativity of $C = 2g^2/(\kappa\gamma) = 150$. Equivalently, the β factor[30] is $\beta = 2C/(2C + 1) = 99.7\%$. A high cooperativity is achieved on all QDs within the spectral window of the microcavity (Fig. 2h).

To probe the coherence of the coupled photon–exciton system, we look for a photon–atom exchange, that is, a 'vacuum Rabi oscillation'[3,16,31]. We drive the system at a frequency positively detuned from LP1 and record the two-photon autocorrelation $g^{(2)}(\tau)$ (where τ is the delay) without spectral filtering (Fig. 3). Coherent oscillations are observed, and their period, 220 ps, corresponds exactly to 2π divided by the measured frequency splitting of the polaritons at this cavity detuning (see Methods).

These oscillations can be understood in terms of the Jaynes–Cummings ladder (Fig. 3 inset). The laser drives weakly the two-photon transition $|0\rangle \leftrightarrow |2-\rangle$. $|2-\rangle$ decays by emitting two photons. Detection of the first photon leaves the system in a superposition of the eigenstates $|1-\rangle$ and $|1+\rangle$ such that a quantum beat takes place. Detection of the second photon projects the system into the ground state $|0\rangle$, stopping the quantum beat (Supplementary Information section II). The large $g^{(2)}(0)$ (80 in this experiment) confirms that the photon states with quanta $n \geq 2$ are preferentially scattered[10,13].

The measured $g^{(2)}(\tau)$ is fully described by a numerical solution of the Jaynes–Cummings model: the standard Hamiltonian, along with the parameters determined by the spectroscopy experiments (Supplementary Information section I), gives excellent agreement with the experimental result (Fig. 3). The vacuum Rabi oscillations are sensitive to decoherence—not just to the loss processes, but also to pure dephasing of the emitter. Including pure dephasing into the theory improves slightly the quantitative description of $g^{(2)}(\tau)$: the pure dephasing rate is $(10 \pm 2)\%$ of the measured linewidth (Supplementary Information section I.F).

The photon statistics change a lot as a function of both laser detuning, Δ_L, and cavity detuning, Δ_C (both defined with respect to the bare exciton). For $\Delta_C = 0$, $g^{(2)}(0)$ is highly bunched at the two-photon resonance, $\Delta_L = -g/\sqrt{2}$ (Fig. 4b), but highly anti-bunched at the single-photon resonance, $\Delta_L = -g$ (Fig. 4c). The anti-bunching is a demonstration of photon blockade[2]. When driving $|0\rangle \leftrightarrow |1-\rangle$, $g^{(2)}(0)$ is limited by the weak two-photon resonance to the $|2-\rangle$ state.
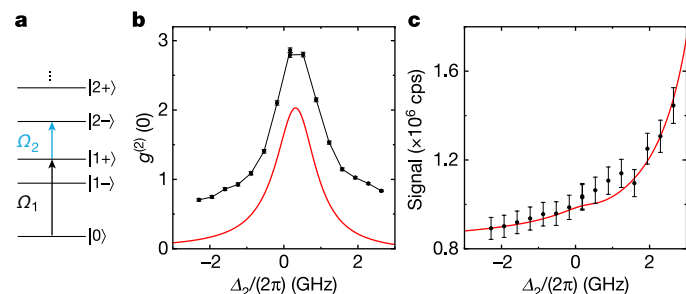
Fig. 5 | Photon-statistics spectroscopy. a, Laser 1 is on resonance with the $|0\rangle \leftrightarrow |1+\rangle$ transition (black arrow; detuning $\Delta_1 = 0$); laser 2 is scanned across the $|1+\rangle \leftrightarrow |2-\rangle$ transition (blue arrow; detuning Δ_2). **b**, $g^{(2)}(0)$ versus Δ_2, showing a pronounced resonance at $\Delta_2 = 3\Delta_C/2 - \Delta_1$. The red solid line is the result of an analytical calculation based on the Jaynes–Cummings Hamiltonian (Supplementary Information section III) with Rabi couplings $\Omega_1/(2\pi) = 0.05$ GHz and $\Omega_2/(2\pi) = 0.45$ GHz. The offset in the experimental data with respect to the theory reflects additional coincidences arising from off-resonant, two-photon absorptions not included in the model. **c**, Signal versus Δ_2. The signal increases with increasing Δ_2 owing to off-resonant driving of the $|0\rangle \leftrightarrow |1-\rangle$ transition by laser 2. Error bars in **b**–**c** are one standard error. All data are from X^0 in QD2 at $B = 0.50$ T; $\Delta_C/(2\pi) = 0.31$ GHz, $\Delta_1/(2\pi) = 0.17$ GHz.

This interpretation is confirmed by the weak oscillations in $g^{(2)}(\tau)$ (Fig. 4c), which are established upon the decay of $|2-\rangle$. Further confirmation of this interpretation is provided by QD3, for which g is larger. This increases the detuning of the two-photon transition and thereby weakens it. For QD3, we find a lower value of $g^{(2)}(0)$, $g^{(2)}(0) = 0.09$. The Jaynes–Cummings model reproduces $g^{(2)}(\tau)$ at the photon blockade, both for $g^{(2)}(0)$ and for the fast oscillations.

The full dependence of $g^{(2)}(0)$ on Δ_L is plotted in Fig. 4e. In principle, $g^{(2)}(0)$ rises to extremely high values[2] as $\Delta_L \to 0$. In practice, the scattered signal becomes weaker and weaker as $\Delta_L \to 0$, so that $g^{(2)}(0)$ reaches a peak and is then pulled down by the Poissonian statistics of the small leakage of laser light into the detector channel (Fig. 4e). $g^{(2)}(\tau)$ is a rich function: its Fourier transform shows in general three frequencies, corresponding to $2g$ (see Supplementary Information section II.D.3), $|g - \Delta_L|$ and $|g + \Delta_L|$ (Fig. 4d, g). All this complexity is described by the Jaynes–Cummings model, which gives excellent agreement with the experimental $g^{(2)}(\tau)$ in all respects.

As the laser power increases, there is a spectral resonance at the first-to-second-rung transitions, LP2 and UP2, and a strong resonance at $\Delta_L = 0$ at the highest powers (Fig. 4a). This is also in precise agreement with the Jaynes–Cummings model (Fig. 4a) and reflects the bosonic enhancement of the transitions between the higher-lying rungs of the Jaynes–Cummings ladder. At the highest powers, $\langle n \rangle \approx 1.7$ when driving LP1 or UP1, increasing to $\langle n \rangle \approx 1.6$ when driving at the bare-cavity frequency. This experiment provides an opportunity to measure the quantum efficiency of the system. Given the success of the Jaynes–Cummings model, we can calculate at each laser power the decay rate through the top mirror and hence the expected signal (see Methods). The quantum efficiency of the entire system—that is, from an exciton in the QD to a 'click' on the detector—is 8.6%. Importantly, of those photons exiting the top mirror and passing through the dark-field optics, almost all (~94%) make their way into the collection fibre (see Methods). This demonstrates experimentally that the microcavity output is close to a simple Gaussian beam.

In the experiments with a single laser, the second rung of the Jaynes–Cummings ladder is accessed by tuning the laser to a two-photon resonance (Fig. 4b). An alternative is to drive the system with two lasers in a pump–probe scheme. The strong transitions arise from the symmetric-to-symmetric and antisymmetric-to-antisymmetric couplings (for example, $|1-\rangle \leftrightarrow |2-\rangle$ and $|1+\rangle \leftrightarrow |2+\rangle$), which lead to measurable changes in the populations of the states[6]. Here we employ an

alternative, photon-statistics spectroscopy, implementing a theoretical proposal[18], and we present this experiment for the symmetric-to-asymmetric $|1+\rangle \leftrightarrow |2-\rangle$ transition. The square of the matrix element is just 3% of that associated with the $|1+\rangle \leftrightarrow |2+\rangle$ transition. A pump laser drives the $|0\rangle \leftrightarrow |1+\rangle$ transition on resonance, and a probe laser, which is highly red-detuned with respect to the pump, is scanned in frequency to locate the $|1+\rangle \leftrightarrow |2-\rangle$ transition (Fig. 5a). There is no resonance in the scattered intensity (Fig. 5c), and any resonances lie in the noise (a few per cent). However, there is a clear resonance in $g^{(2)}(0)$ at exactly the expected frequency of $\Delta_2 = 3\Delta_C/2 - \Delta_1$ (Fig. 5b): at the weak $|1+\rangle \leftrightarrow |2-\rangle$ transition the number of scattered photons hardly changes, but there are profound changes in their statistical correlations. Again, the Jaynes–Cummings model describes the experiment well (Fig. 5b, c). Here, a short-time expansion in a truncated Hilbert space (first two rungs of the Jaynes–Cummings ladder) is used to calculate $g^{(2)}(0)$ (Supplementary Information section III).

As an outlook, we offer some perspectives for future development. (a) The device is a potentially excellent single-photon source. For fixed g and γ, the efficiency of photon extraction via the cavity can be maximized by satisfying the condition $\kappa = 2g$ (see Methods). Taking the maximum g reported here, this corresponds to $Q = 3.7 \times 10^4$, which can be achieved with the semiconductor mirror used here and a top mirror with reduced reflectivity. At this relatively low Q, the residual absorption losses in the semiconductor are negligible and, following exciton creation, the efficiency of photon extraction via the top mirror should be as high as 94%. This concept can be profitably combined with lateral excitation, an 'atom drive'[3,32] and spin control for the creation of shaped-waveform single photons. (b) The system opens a route towards a photon–photon gate. A key advance here is the coherent exciton–photon interaction, which can be potentially exploited in the Duan–Kimble scheme[5]. Reducing the intrinsic cavity loss by a factor of ten (which is feasible with a more advanced semiconductor design with narrower gates, for instance), the fidelity could be maximized to $F_{pp} = 92\%$ by choosing $\kappa/(2\pi) = 3.8$ GHz (Supplementary Information section IV.D). For both (a) and (b), cavity mode splitting can be eliminated by applying a bias across the semiconductor DBR[33], and a monolithic device could use strain tuning of the QD. On the basis of these considerations, a compact, on-chip, high-cooperativity single-photon–single-QD interface is within reach.

Online content

Any methods, additional references, Nature Research reporting summaries, source data, extended data, supplementary information, acknowledgements, peer review information; details of author contributions and competing interests; and statements of data and code availability are available at https://doi.org/10.1038/s41586-019-1709-y.

1. Boca, A. et al. Observation of the vacuum Rabi spectrum for one trapped atom. *Phys. Rev. Lett.* **93**, 233603 (2004).
2. Birnbaum, K. et al. Photon blockade in an optical cavity with one trapped atom. *Nature* **436**, 87–90 (2005).
3. Hamsen, C., Tolazzi, K. N., Wilk, T. & Rempe, G. Two-photon blockade in an atom-driven cavity QED system. *Phys. Rev. Lett.* **118**, 133604 (2017).
4. Zheng, S.-B. & Guo, G.-C. Efficient scheme for two-atom entanglement and quantum information processing in cavity QED. *Phys. Rev. Lett.* **85**, 2392–2395 (2000).
5. Duan, L.-M. & Kimble, H. J. Scalable photonic quantum computation through cavity-assisted interactions. *Phys. Rev. Lett.* **92**, 127902 (2004).
6. Fink, J. M. et al. Climbing the Jaynes–Cummings ladder and observing its √n nonlinearity in a cavity QED system. *Nature* **454**, 315–318 (2008).
7. Kawasaki, A. et al. Geometrically asymmetric optical cavity for strong atom–photon coupling. *Phys. Rev. A (Coll. Park)* **99**, 013437 (2019).
8. Reithmaier, J. et al. Strong coupling in a single quantum dot-semiconductor microcavity system. *Nature* **432**, 197–200 (2004).
9. Yoshie, T. et al. Vacuum Rabi splitting with a single quantum dot in a photonic crystal nanocavity. *Nature* **432**, 200–203 (2004).
10. Faraon, A. et al. Coherent generation of non-classical light on a chip via photon-induced tunnelling and blockade. *Nat. Phys.* **4**, 859–863 (2008).
11. Hennessy, K. et al. Quantum nature of a strongly coupled single quantum dot-cavity system. *Nature* **445**, 896–899 (2007).

12. Rakher, M. T., Stoltz, N. G., Coldren, L. A., Petroff, P. M. & Bouwmeester, D. Externally mode-matched cavity quantum electrodynamics with charge-tunable quantum dots. *Phys. Rev. Lett.* **102**, 097403 (2009).
13. Reinhard, A. et al. Strongly correlated photons on a chip. *Nat. Photon.* **6**, 93–96 (2012).
14. Volz, T. et al. Ultrafast all-optical switching by single photons. *Nat. Photon.* **6**, 605–609 (2012).
15. Ota, Y. et al. Large vacuum Rabi splitting between a single quantum dot and an H0 photonic crystal nanocavity. *Appl. Phys. Lett.* **112**, 093101 (2018).
16. Kuruma, K., Ota, Y., Kakuda, M., Iwamoto, S. & Arakawa, Y. Time-resolved vacuum Rabi oscillations in a quantum-dot–nanocavity system. *Phys. Rev. B* **97**, 235448 (2018).
17. Greuter, L., Starosielec, S., Kuhlmann, A. V. & Warburton, R. J. Towards high-cooperativity strong coupling of a quantum dot in a tunable microcavity. *Phys. Rev. B* **92**, 045302 (2015).
18. Schneebeli, L., Kira, M. & Koch, S. W. Characterization of strong light-matter coupling in semiconductor quantum-dot microcavities via photon-statistics spectroscopy. *Phys. Rev. Lett.* **101**, 097401 (2008).
19. Stockklauser, A. et al. Strong coupling cavity QED with gate-defined double quantum dots enabled by a high impedance resonator. *Phys. Rev. X* **7**, 011030 (2017).
20. Mi, X., Cady, J. V., Zajac, D. M., Deelman, P. W. & Petta, J. R. Strong coupling of a single electron in silicon to a microwave photon. *Science* **355**, 156–158 (2017).
21. Samkharadze, N. et al. Strong spin-photon coupling in silicon. *Science* **359**, 1123–1127 (2018).
22. Landig, A. J. et al. Coherent spin–photon coupling using a resonant exchange qubit. *Nature* **560**, 179–184 (2018).
23. Somaschi, N. et al. Near-optimal single-photon sources in the solid state. *Nat. Photon.* **10**, 340–345 (2016).
24. Ding, X. et al. On-demand single photons with high extraction efficiency and near-unity indistinguishability from a resonantly driven quantum dot in a micropillar. *Phys. Rev. Lett.* **116**, 020401 (2016).
25. Guha, B. et al. Surface-enhanced gallium arsenide photonic resonator with quality factor of 6×10^6. *Optica* **4**, 218–221 (2017).
26. Kuhlmann, A. V. et al. Charge noise and spin noise in a semiconductor quantum device. *Nat. Phys.* **9**, 570–575 (2013).
27. Högele, A. et al. Voltage-controlled optics of a quantum dot. *Phys. Rev. Lett.* **93**, 217401 (2004).
28. Casey, H. C., Sell, D. D. & Wecht, K. W. Concentration dependence of the absorption coefficient for n- and p-type GaAs between 1.3 and 1.6 eV. *J. Appl. Phys.* **46**, 250–257 (1975).
29. Kuhlmann, A. V. et al. A dark-field microscope for background-free detection of resonance fluorescence from single semiconductor quantum dots operating in a set-and-forget mode. *Rev. Sci. Instrum.* **84**, 073905 (2013).
30. Kuhn, A. & Ljunggren, D. Cavity-based single-photon sources. *Contemp. Phys.* **51**, 289–313 (2010).
31. Kasprzak, J. et al. Up on the Jaynes–Cummings ladder of a quantum-dot/microcavity system. *Nat. Mater.* **9**, 304–308 (2010).
32. Law, C. & Kimble, H. Deterministic generation of a bit-stream of single-photon pulses. *J. Mod. Opt.* **44**, 2067–2074 (1997).
33. Frey, J. A. et al. Electro-optic polarization tuning of microcavities with a single quantum dot. *Opt. Lett.* **43**, 4280–4283 (2018).

Article

Methods

Design and growth of the heterostructure

The heterostructure is grown by molecular beam epitaxy. It consists of an n–i–p diode with embedded self-assembled InAs QDs grown on top of an AlAs/GaAs DBR with nominal (measured) centre wavelength of 940 nm (920 nm).

The growth on a (100)-oriented GaAs wafer is initiated by a quarter-wave layer (QWL) of an AlAs/GaAs short-period superlattice (18 periods of 2.0-nm-thick GaAs and 2.0-nm-thick AlAs) for stress relief and surface smoothing. The growth continues with 46 pairs of GaAs (67.9 nm) and AlAs (80.6 nm) QWLs forming the 'bottom' DBR. The active part of the device consists of a QWL of GaAs (69.8 nm) followed by a 41.0-nm-thick layer of Si-doped GaAs (n^+, 2×10^{18} cm^{-3}), the back gate. 25.0 nm of undoped GaAs, the tunnel barrier, is subsequently grown, after which InGaAs QDs are self-assembled using the Stranski–Krastanow process and a flushing step[34] to blue-shift the QD emission. The layer thicknesses are such that the QDs are located at an antinode of the vacuum electric field. The QDs are capped with an 8.0-nm-thick layer of GaAs. The growth proceeds with an $Al_{0.33}Ga_{0.67}As$ layer (190.4 nm) used as a blocking barrier to reduce the current flow through the diode structure. The heterostructure is completed by 25.0-nm-thick C-doped GaAs (5.0 nm p^+, 2×10^{18} cm^{-3} and 20.0 nm p^{++}, 1×10^{19} cm^{-3}), the top gate, and finally a 54.6-nm-thick GaAs capping layer. The heterostructure is shown in Extended Data Fig. 1.

The top gate is centred around a node of the standing wave of the vacuum electric field to minimize free-carrier absorption from the p-doped GaAs. A condition on the tunnel barrier thickness (it is typically less than 40 nm thick to achieve a non-negligible tunnel coupling with the Fermi sea) prevents the back gate from being positioned similarly at a vacuum field node. However, the free-carrier absorption of n^+-doped GaAs is much smaller than that of p^{++}-doped GaAs at a photon energy of 1.3 eV (absorption coefficient $\alpha \approx 10$ cm^{-1} for n^+-doped GaAs compared to $\alpha \approx 70$ cm^{-1} for p^{++}-doped GaAs)[28]. We exploit the weak free-carrier absorption of n^+-doped GaAs and use a standard 25-nm-thick tunnel barrier. The back gate is thus positioned close to the node of the vacuum electric field but is not centred around the node itself.

Post-growth processing

After growth, individual 2.5×3.0 mm^2 pieces are cleaved from the wafer. The QD density decreases from about 10^{10} cm^{-2} to zero in an approximately centimetre-wide stripe across the wafer. The sample used in these experiments was taken from this stripe and has a density of 7×10^6 cm^{-2}. (The QD density was measured by photoluminescence imaging.)

Separate Ohmic contacts are made to the n^+ and p^{++} layers and a passivation layer is added to the surface. To contact the n^+ layer (the back gate), a local etch in citric acid is used to remove the capping layer, the p^{++} layer, as well as parts of the blocking barrier. NiAuGe is deposited on the new surface by electron-beam physical vapour deposition (EBPVD). Low-resistance contacts to the n^+ layer are formed by thermal annealing. To contact the p^{++} layer (the top gate), another local etch removes the capping layer. A 100-nm-thick Ti/Au contact pad is deposited on the new surface using EBPVD. This contact is not thermally annealed but nevertheless provides a reasonably low-resistance contact to the top gate (Extended Data Fig. 1a).

Following the fabrication of the contacts to the back and top gates, the contacts themselves are covered with photoresist, and the surface of the sample is passivated by chemical treatment. HCl removes a thin oxide layer and a few nanometres of GaAs on the sample surface. After rinsing the sample with deionized water, it is immediately put into an ammonium sulphide ((NH$_4$)$_2$S) bath and subsequently into an atomic layer deposition chamber, where 8 nm of Al$_2$O$_3$ is deposited at a temperature of 150 °C. This process is essential for the present device to reduce surface-related absorption, as a high Q factor is achieved only with a surface passivation layer. We can only speculate on the microscopic explanation of this effect. The passivation procedure reduces the surface density of states, leading to an unpinning of the Fermi energy at the surface. On the one hand, this reduces the Franz–Keldysh absorption in the capping layer; on the other hand, it reduces the absorption from mid-gap surface states. A clear advantage of the surface passivation is that native oxides of GaAs are removed and prevented from re-forming; this not only reduces the probability of surface absorption but also provides a robust and stable termination to the GaAs sample[25].

The sample holder contains large Au pads, and Ti/Au and NiAuGe films are connected to the Au pads by wire bonding. Silver paint is used to connect the Au pads to macroscopic wires (twisted pairs).

CO$_2$ laser ablation of the curved mirror

The template for the curved top mirror is produced by in-house CO$_2$ laser ablation[35,36] on a 0.5-mm-thick fused-silica substrate. The radius of curvature of the indentation is 10.5 μm, as measured by confocal scanning microscopy[36], and the depth relative to the unprocessed surface is 1.2 μm. After laser ablation, the template is coated with 22 pairs of Ta$_2$O$_5$ (refractive index $n = 2.09$) and SiO$_2$ ($n = 1.46$) layers (terminating with a layer of SiO$_2$) by ion-beam sputtering[37].

Mirror characterization

Each mirror is characterized by measuring the reflected light intensity at wavelengths outside the stopband. The reflection oscillates as a function of wavelength. We find that these oscillations are a sensitive function of the exact layer thicknesses of the DBR. The transmission is simulated with a one-dimensional transfer matrix calculation, for instance, the Essential Macleod package. A fit is generated, taking the nominal growth parameters as the starting point and making the simplest possible assumption to describe systematic differences between the experimental results and the calculation. In this way, we find that the GaAs (AlAs) layers in the semiconductor DBR start with a physical thickness of 64.6 nm (80.2 nm) for $n = 3.49$ ($n = 2.92$), reducing linearly to 63.9 nm (79.8 nm). The change arises simply because the growth rate changes slightly during the long process of growing the DBR. Accordingly, we anticipate that the layers in the active layer have actual thicknesses of 38.9 nm (n^+ layer), 29.4 nm (tunnel barrier), 183.3 nm (blocking barrier), 19.0 nm (p^{++} layer), 4.8 nm (p^+ layer) and 55.8 nm (cap). The main consequence of the slight change in growth rate during the growth is that the stopband centre is shifted from 940 nm (design wavelength) to 920 nm. The maximum reflectivity at the stopband centre is not changed substantially by these slight deviations in layer thicknesses.

For technical reasons, the dielectric DBR has a nominal (measured) stopband centre of 1,017 nm (980 nm), that is, it is red-detuned from the QD emission. Because the transmission could not be measured during deposition at a wavelength of 940 nm, a modified quarter-wave stack was chosen, which is expected to have similar transmission (87 ppm) at 1,064 nm and 940 nm. A laser at 1,064 nm was used for in situ characterization. The displacement in the stopband centres between the top and bottom DBRs was an issue only at wavelengths below 915 nm, where the cavity Q factor decreases rapidly with decreasing wavelength. Matching of the two stopband centres would give a high Q factor over a larger spectral range.

Microcavity characterization

A microcavity was constructed using a planar dielectric mirror and the curved dielectric mirror used for the main QD experiment. Both planar and curved silica templates were coated in the same run. With the smallest possible mirror separation of $3\lambda/2$ (limited by the indentation depth of the curved mirror) we determine Q factors of 1.7×10^5 (1.5×10^6) at 920 nm (980 nm) at room temperature. The fundamental microcavity mode splits into a doublet with orthogonal polarizations; at a wavelength of 920 nm, this splitting is typically 13 GHz. These measurements demonstrate the very high quality of the dielectric mirror, in particular the curved dielectric mirror.

The microcavity consisting of the semiconductor mirror and the same curved dielectric mirror has a Q factor of typically 5×10^5 at 920 nm at 4.2 K (Fig. 2), a factor of about 3 larger than the dielectric DBR–dielectric DBR microcavity described above. This increase can be explained by the larger (by a factor of 2) effective cavity length of the semiconductor–dielectric cavity (the group delay of the semiconductor mirror is larger than that of a dielectric mirror owing to the $3\lambda/2$-thick active layer) and the larger (by a factor of 1.5) finesse. This increase in finesse suggests that at 920 nm the reflectance of the semiconductor mirror is higher than that of the dielectric mirror.

The fundamental mode at a wavelength of 920 nm has a typical polarization splitting of 32 GHz—larger than the polarization splitting of the dielectric DBR–dielectric DBR microcavity (13 GHz at 920 nm). This suggests that the main origin of the polarization splitting is birefringence in the semiconductor induced by strain (AlAs is not exactly lattice-matched to GaAs).

Low-temperature setup and stability
Both the top mirror and the GaAs sample are firmly glued to individual titanium sample holders and mounted inside a titanium 'cage' (Extended Data Fig. 1a)[38]. The holder for the GaAs sample is fixed to a stack of piezo-driven XYZ nano-positioners, whereas the top-mirror holder is fixed to the titanium cage via soft (indium) washers, which act as a flexible material for tilt alignment at room temperature. By observing the cavity with a conventional optical microscope and tightening each screw of the mirror holder individually, Newton rings appear between the two mirrors, which can be centred to ensure mirror parallelism at room temperature. The entire microcavity setup is then inserted in another titanium cage. This outer cage is connected to an optical cage system inside a vacuum tube. The tube is evacuated, flushed with He exchange gas (25 mbar), pre-cooled in liquid nitrogen, and finally transferred into the helium bath cryostat.

To minimise the exposure of the microcavity to acoustic noise, the cryostat is decoupled from floor vibrations via both active and passive isolation platforms (Extended Data Fig. 1b). An acoustic enclosure surrounds both the entire cryostat and the microscope, providing a shield against airborne acoustic noise (Extended Data Fig. 1b). There is no active-feedback mechanism acting on the z-piezo element of the microcavity. Nevertheless, a root-mean-square cavity-length fluctuation[36] of about 0.5 pm is measured in the best case, limiting our Q factors to $Q \approx 2.0 \times 10^6$. This corresponds to our highest measured Q factor of $Q = 1.6 \times 10^6$ in the case of a microcavity consisting of the curved top mirror paired with a dielectric bottom mirror of identical coating. This suggests that in the case of the combination of a GaAs sample and a curved dielectric mirror, the Q factor is only slightly reduced by environmental noise.

QD charging
To characterize QD charging, photoluminescence measurements were performed using non-resonant excitation at a wavelength of 830 nm as a function of the voltage applied between the top and bottom gates. Extended Data Fig. 2a shows such a photoluminescence charge map, taken on the sample without the top mirror. Both positive (X^+) and negative (X^-) trions, as well as the neutral exciton (X^0), were identified. The charge states of a QD within the cavity can be recorded in a similar way. To detect all the photoluminescence before filtering by the cavity, a sine wave voltage was applied to the z-piezo element of the cavity so that the cavity was continuously scanned through one free spectral range per integration time window of the spectrometer.

Cross-polarized detection of resonance fluorescence
The behaviour of each QD under resonant excitation can be investigated by suppressing back-reflected laser light in the detection arm and detecting the resonance fluorescence (RF). We achieve this with a dark-field technique[29]. The optical components are shown in Extended

Data Fig. 1b. The excitation laser passes through a linear polarizer with polarization matched to the reflection of the lower polarizing beam-splitter (PBS). The two PBSs transmit the orthogonal polarization in the vertical direction, the detection channel. The final polarizing element of the excitation channel and the first polarizing element of the detection channel is a quarter-wave plate, which has a dual function. First, by setting the angle of the quarter-wave plate to 45°, the microscope can be operated also in bright-field mode. This is very useful for alignment purposes and for optimization of the out-coupling efficiency. Second, in dark-field mode, the quarter-wave plate allows very small retardances to be introduced, correcting for the slight ellipticity in the excitation polarization state[29]. The quarter-wave plate allows extremely high bright-field-to-dark-field extinction ratios to be achieved. The microscope can be operated in a set-and-forget mode—once the polarizer and wave plate are aligned, the laser suppression is maintained in the original setup over days[29] and even weeks in this case. This very robust operation (despite the fact that control of the wave-plate rotation at the millidegree level is necessary)[29] is likely to be a consequence of the effective damping of acoustic and vibrational noise acting on the microscope head in the cavity experiment.

Second-order correlation measurements and single-photon detectors
Second-order correlation measurements are performed with a Hanbury Brown–Twiss (HBT) setup. The signal from the detection fibre (Extended Data Fig. 1b) is sent to a 50:50 fibre beam-splitter and then to two superconducting nanowire single-photon detectors (SNSPDs; Single Quantum Eos). In these experiments, all the photons from the experiment are sent to the HBT setup (no spectral selection is employed). Each SNSPD has a detector efficiency of $\eta_{detector} \approx 85\%$ and a negligible dark count rate of 10–40 cps. The total timing resolution in the $g^{(2)}$ mode includes the timing resolution of both SNSPDs and the resolution of the time-tagging hardware. In total, it is about 35 ps (full-width at half-maximum), which is well below the vacuum Rabi periods measured in this work.

The dead time of the time-tagging hardware is about 95 ns, which sets a limit for the maximally detectable count rate. To measure count rates higher than about 5×10^6 cps per detector, the 1% arm of the detection fibre is used instead of the 99% arm, and the number of counts is calibrated accordingly.

For the evaluation of $g^{(2)}(\tau)$ we use a time window of 100 ns. For all presented $g^{(2)}(\tau)$ data, we use a bin size of 4 ps. For all presented $g^{(2)}(0)$ values, we perform an FFT of $g^{(2)}(\tau)$ (bin size of 16 ps), then cut all frequency components above 14 GHz and calculate the inverse FFT. In this way, we make sure that the $g^{(2)}(0)$ values are averaged over a time of 35 ps, which is large with respect to the original binning of 16 ps but small with respect to the period of the vacuum Rabi oscillations.

Neutral exciton
An RF scan of QD5 without the top mirror is shown in Extended Data Fig. 2b. In this case, the detuning between the QD and the laser is controlled by fixing the laser frequency and scanning the gate voltage, which detunes the QD resonance frequency via the d.c. Stark shift. Two peaks are observed from the neutral exciton, X^0. The splitting corresponds to the FSS. By taking several scans for different laser frequencies, a d.c. Stark shift of 240 GHz V^{-1} is determined for this QD. The measured full-width at half-maximum of each neutral exciton peak corresponds to 0.32 GHz, a value close to the typical transform limit of 0.25 GHz for these InGaAs QDs at a wavelength of 940 nm (ref. [39]).

Polarization axes
The X^0 polarization axis (hereafter, 'axis') varies among QDs. The cavity also has an axis. A complication is that the cavity mode splitting (32 GHz), the X^0 fine structure (1–10 GHz) and the frequency separating the two polaritons in the strong-coupling regime (6–9 GHz) are

all similar. Extended Data Fig. 3a shows an example: full RF scans of the cavity-coupled QD1 are shown, together with their respective line cuts at zero cavity detuning (Extended Data Fig. 3b, f, j). The fundamental cavity mode splits into two modes with linear and orthogonal polarizations. At zero magnetic field ($B = 0.00$ T) the neutral exciton X^0 also splits into two lines with linear and orthogonal polarizations. In the case of QD1 at $B = 0.00$ T, the X^0 and cavity axes are close to parallel, such that one X^0 line couples strongly to one cavity mode and weakly to the other cavity mode, and vice versa for the other X^0 line (Extended Data Fig. 3a). The line cut at one particular cavity frequency shows the polaritons and a weak feature between them (Extended Data Fig. 3b). The analysis including both cavity modes and two X^0 transitions establishes that in Extended Data Fig. 3b the two polaritons arise from strong coupling between one X^0 transition and one cavity mode. The central feature arises from an out-of-resonance response of the strong coupling between the other X^0 transition and the other cavity mode. The bare-cavity mode is not observed at all in the spectral range of Extended Data Fig. 3a.

The QD–cavity couplings in this experiment can be selected in a few ways. First, the X^0 axis varies among QDs. It is not difficult to find a QD with an axis matching closely that of the cavity, so that one X^0 line interacts primarily with one cavity mode and the other X^0 line interacts primarily with the other cavity mode. Extended Data Fig. 3a depicts an example of this behaviour.

Second, application of a small magnetic field pushes the two X^0 lines apart in frequency. At a magnetic field of $B = 0.40$ T, the X^0 lines (QD1) are separated by 12 GHz, so if one X^0 line is resonant with the microcavity, the other X^0 line is far detuned. Extended Data Fig. 3b, f shows an example. In such magnetic fields, the X^0 lines become circularly polarized, so the X^0 axis no longer has a role. The price to pay is a reduction in the coupling parameter g by a factor of $\sqrt{2}$ with respect to the optimal value at zero magnetic field (Extended Data Fig. 3f).

Third, the FSS disappears upon switching to a charged exciton, either X^- or X^+; there is just one peak at zero magnetic field (Extended Data Fig. 3i, j), a Zeeman-split doublet at finite magnetic field.

To exploit all three options, we use the power of in situ cavity detuning. When applying a magnetic field or changing the voltage applied to the device, the QD optical frequency changes by many cavity linewidths, but in each case the cavity can be brought into resonance.

Vacuum Rabi frequency versus cavity detuning

Figure 3 shows $g^{(2)}(\tau)$ as a function of delay τ for a cavity detuned by $\Delta_C = 0.73g$ with respect to the emitter. Here we show that vacuum Rabi oscillations in $g^{(2)}(\tau)$ are observed for different values of Δ_C and that the frequency of these oscillations changes according to the change in polariton splitting in the $|1\pm\rangle$ manifold for different values of Δ_C (see Extended Data Fig. 4 and Supplementary Information section V for analytical calculations for the case of $\Delta_C = 0$). The dashed vertical line in Extended Data Fig. 4 depicts the cavity detuning for the data shown in Fig. 3. Consistent with the excellent agreement of the numerical model for $g^{(2)}(\tau)$ with the experiment, an analytical approach to determine the vacuum Rabi period yields $T = 220$ ps, in exact agreement with the experimental observations.

$g^{(2)}(0)$ versus laser and cavity detuning

In the experiment, three frequencies can be tuned in situ: the laser frequency ω_L, the emitter frequency ω_X (via the gate voltage) and the cavity frequency ω_C (via tuning of the cavity length).

Figure 4e shows $g^{(2)}(0)$ as a function of laser detuning Δ_L for a cavity detuning of $\Delta_C = 0$ on QD2 at $B = 0.50$ T. $g^{(2)}(0)$ can be described well by the model and a small laser background. This point is investigated also in other cases. Extended Data Fig. 3c, g, h shows more $g^{(2)}(0)$ measurements of the neutral exciton of QD1 at $B = 0.00$ T and 0.40 T, with close-to-zero cavity detuning (Extended Data Fig. 3c, g) and a cavity detuning of $\Delta_C \approx g$ (Extended Data Fig. 3h).

The in situ tunability of the microcavity can be exploited in an alternative experiment, in which the cavity is detuned and the polaritons are driven resonantly at each cavity detuning. Extended Data Fig. 5a, b shows the behaviour of the first-rung polaritons (LP1 in black, UP1 in red) as a function of Δ_C. Also in this case, the model reproduces the experimental results well. The reason for the slight discrepancy in the $g^{(2)}(0)$ values of the lower polariton at large and negative Δ_C is the fact that the laser starts driving the second fine-structure level, which is weakly coupled to the same cavity mode. This increases slightly the number of single photons in the detection signal, as evidenced by the slight anti-bunching in the experimental data.

Power dependence

The experiments in Figs. 1–5, Extended Data Figs. 3a–c, e–j, 5a, b are all recorded with a weak driving laser, that is, with a mean photon number in the cavity well below 1. We present here the observed behaviour of the system as the power of the driving laser increases.

In Extended Data Fig. 5c we plot the measured and calculated scattering signal measured when driving LP1 (black) and UP1 (red) with increasing excitation power. A striking feature is that the system does not saturate (Extended Data Fig. 5c). This is evidence that the full ladder of Jaynes–Cummings levels exists. To model this power dependence, it is necessary to determine the connection between the Rabi frequency Ω, the input parameter to the model, and the laser power P, the control parameter in the experiment. Clearly, $\Omega \propto \sqrt{P}$. At the lowest powers, only the zeroth and first rungs of the Jaynes–Cummings ladder are populated, so that the $|0\rangle \leftrightarrow |1-\rangle$ and $|0\rangle \leftrightarrow |1+\rangle$ transitions behave like two-level systems: the scattered signal increases linearly with laser power, as expected (Extended Data Fig. 5c).

We parameterize the link between Ω and P by adopting the link for a two-level system, namely $\Omega = \sqrt{\frac{P}{P_0} \frac{\kappa + \gamma}{2} \frac{1}{\sqrt{2}}}$, where P is the laser power (monitored at the 50:50 fibre beam-splitter) and P_0 is a reference power. The signal S is equal to the steady-state photon occupation in the cavity multiplied by the cavity loss rate (κ) and the cavity-to-detector system efficiency (η_{system}), $S = \eta_{system}\kappa\langle n\rangle$. We calculate $\langle n\rangle$ from the Jaynes–Cummings model with the parameters g, κ and γ determined from the spectroscopy experiment and $(\Delta_C, \Delta_L) = (0, \pm g)$.

The nonlinear power dependence (Extended Data Fig. 5c) enables both P_0 and η_{system} to be determined. A fit to the experimental data leads to $P_0 = 214$ nW ($P_0 = 529$ nW) for LP1 (UP1) and $\eta_{system} = 12\%$. The difference in P_0 for LP1 and UP1 results in unequal polariton populations at constant input powers, as seen in Fig. 2f, g. The difference in P_0 values probably arises from a polarization-dependent chromaticity in the throughput of the excitation channel of the microscope . The same model gives excellent agreement with the experimental $g^{(2)}(0)$ for both LP1 and UP1 (Extended Data Fig. 5d, e).

The behaviour of the system as a function of driving power can also be explored by measuring the Δ_L dependence of the scattered intensity for $\Delta_C = 0$. Extended Data Fig. 3d, k shows power-dependent RF scans acquired when the bare exciton and cavity are resonant. At low power, LP1 and UP1 are clearly resolved. At higher power, bumps appear at the two-photon LP2 and UP2 resonances. In Extended Data Fig. 3k, there is no resonance close to the bare-cavity mode at low power, enabling us to explore fully the behaviour of the system, even at very large driving powers. At the highest powers, the response is dominated by a feature at $\Delta_L \approx 0$ (Extended Data Fig. 3k). This too is evidence that the full Jaynes–Cummings ladder can be accessed. At the highest powers, the system 'climbs' the Jaynes–Cummings ladder because of the bosonic enhancement of photons, so that the average photon occupation is large and the polariton resonances become closer in frequency to the bare-cavity mode. This power dependence can also be described by the model, and very good agreement is found between our numerical model and the data in Extended Data Fig. 3k. (Owing to the presence of

the second fine-structure level in Extended Data Fig. 3d, our numerical model is incomplete in this case.)

Quantum efficiency

The dependence of the scattered intensity on laser power enables us to determine $\eta_{system} = 12\%$. One contribution to η_{system} is the out-coupling efficiency[23], which is defined as the fraction of photons in the κ channel leaving through the top mirror (rate κ_{top}):

$$\eta_{out} = \frac{\kappa_{top}}{\kappa} \times \frac{T_{top}}{T_{top} + T_{bottom} + A} \tag{1}$$

Using the model of the mirrors, we determine $(T_{top}, T_{bottom}, A) = (116, 1, 373)$ ppm at wavelength $\lambda = 923$ nm. Here, T_{top} (T_{bottom}) and A are the fractional intensity losses per round trip via transmission through the top (bottom) mirror and absorption/scattering losses, respectively. This gives $\eta_{out} = 24\%$.

The system efficiency can be described using a number of additional factors. If the cavity and microscope axes lie at an angle of $\phi = 45°$ to each other, $\eta_{dark\text{-}field} = 50\%$. This is not exactly the case in practice. For X^0 in QD2 ($B = 0.50$ T) it is $\phi = 37° \pm 6°$, resulting in $\eta_{dark\text{-}field} = (63 \pm 10)\%$. Once a photon has entered the detection channel after the dark-field polarization optics, it is coupled into the collection fibre with probability η_{fibre}. Overall,

$$\eta_{system} = \eta_{out} \times \eta_{dark\text{-}field} \times \eta_{fibre} \times \eta_{detector} \tag{2}$$

The detector has a quantum efficiency of $\eta_{detector} = 85\%$. From these results, we find that $\eta_{fibre} = (94^{+6}_{-15})\%$.

The collection fibre is a single-mode optical fibre and supports a propagating Gaussian mode. The high value of η_{fibre} is only achievable with excellent mode matching between the cavity output and the optical fibre, which constitutes experimental proof that the cavity output is described extremely well by a Gaussian mode.

We note that the exciton-to-photon quantum efficiency (the probability of an exciton producing a photon that exits via the κ channel) of the microcavity[40] is

$$\eta_{cavity} = \beta \frac{\kappa}{\kappa + \gamma} \tag{3}$$

which is 72% for QD2 ($B = 0.50$ T). By maximizing η_{cavity} for fixed g and γ (by choosing $\kappa = 2g$), the collection efficiency $\eta_{cavity} \times \eta_{out}$ into the first lens of the optical setup[23,24,41,42] can be as high as 94% with the present microcavity device. The overall exciton-to-detector quantum efficiency is

$$\eta_{exciton} = \eta_{cavity} \times \eta_{system} \tag{4}$$

which is 8.6% in the present experiment.

Data availability
The data that support the findings of this study are available from the corresponding author upon reasonable request.

34. Wasilewski, Z., Fafard, S. & McCaffrey, J. Size and shape engineering of vertically stacked self-assembled quantum dots. *J. Cryst. Growth* **201–202**, 1131–1135 (1999).
35. Hunger, D., Deutsch, C., Barbour, R. J., Warburton, R. J. & Reichel, J. Laser micro-fabrication of concave, low-roughness features in silica. *AIP Adv.* **2**, 012119 (2012).
36. Greuter, L. et al. A small mode volume tunable microcavity: development and characterization. *Appl. Phys. Lett.* **105**, 121105 (2014).
37. The VIRGO Collaboration. The VIRGO large mirrors: a challenge for low loss coatings. *Class. Quantum Gravity* **21**, S935–S945 (2004).
38. Barbour, R. J. et al. A tunable microcavity. *J. Appl. Phys.* **110**, 053107 (2011).
39. Dalgarno, P. A. et al. Coulomb interactions in single charged self-assembled quantum dots: radiative lifetime and recombination energy. *Phys. Rev. B* **77**, 245311 (2008).
40. Cui, G. & Raymer, M. G. Quantum efficiency of single-photon sources in the cavity-QED strong-coupling regime. *Opt. Express* **13**, 9660–9665 (2005).
41. Wang, H. et al. On-demand semiconductor source of entangled photons which simultaneously has high fidelity, efficiency, and indistinguishability. *Phys. Rev. Lett.* **122**, 113602 (2019).
42. Liu, J. et al. A solid-state source of strongly entangled photon pairs with high brightness and indistinguishability. *Nat. Nanotechnol.* **14**, 586–593 (2019).

Author contributions D.N. carried out the surface passivation, the experiments and the detailed data analysis. I.S. developed the numerical model and used it to guide the experiments. P.S. and N.S. developed the analytical theory. M.C.L. contributed to the QD characterization, the dark-field setup and the $g^{(2)}(\tau)$ measurements. S.S. and D.R. developed the microcavity experiment and assisted D.N. in its operation. A.L., D.N., S.S. and R.J.W. designed the heterostructure. S.R.V., R.S., A.D.W. and A.L. fabricated the device for the experiments (molecular beam epitaxy of the heterostructure, post-growth processing of the diode structure). V.D. applied the dielectric coating to the curved-mirror template fabricated by S.S. D.N. and R.J.W. wrote the manuscript with input from all authors.
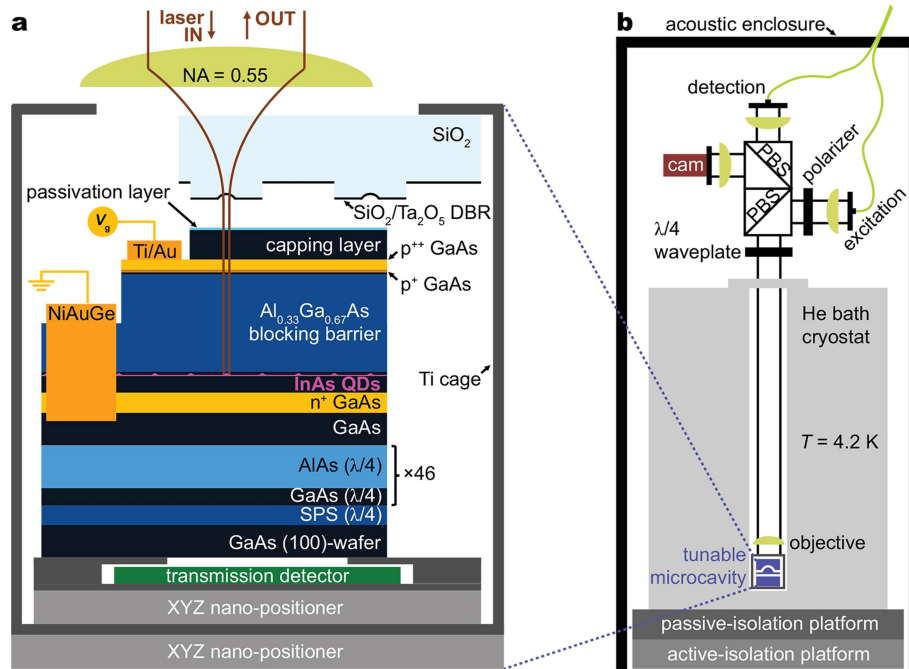
Extended Data Fig. 1 | Tunable-microcavity setup. a, The top mirror is fixed to the upper inner surface of a titanium 'cage'. The sample is mounted on a piezo-driven XYZ nano-positioner, which is fixed to the bottom inner surface of the cage. The nano-positioner allows full in situ spatial and spectral tuning of the microcavity at cryogenic temperatures. The titanium cage resides on another XYZ nano-positioner, enabling close-to-perfect mode matching of the cavity mode to the external laser beam[36]. **b**, An outer Ti cage, containing the inner Ti cage and a second nano-positioner, is fixed to an optical rod system, which is inserted into a vacuum tube filled with He exchange gas. The optical elements depicted in the image (objective lens, quarter-wave plate, two polarizing beam-splitters (PBSs), polarizer, CMOS camera, two fibre couplers) make up the dark-field microscope for near-background-free detection of resonance fluorescence[29]. The back-reflected laser is suppressed by a factor of up to 10^8 by choosing orthogonal polarization states for the excitation and detection channels[29]. The optical fibre attached to the excitation (detection) arm of the microscope includes a 50:50 (99:1) fibre beam-splitter to monitor the laser power sent into the microscope (reflected from the sample). The cryostat sits on both active- and passive-isolation platforms and is surrounded by an acoustic enclosure to minimize acoustic noise. Both images are schematic representations and are not to scale. The exact layer thicknesses and doping concentrations are given in the text.
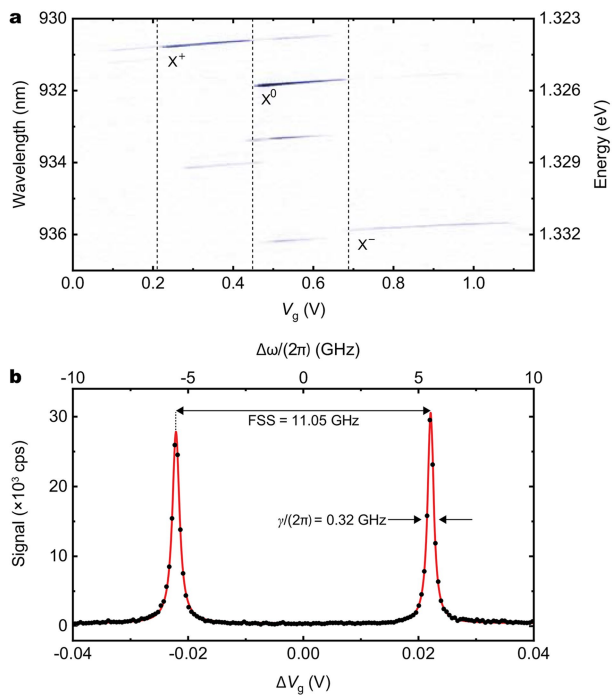
Extended Data Fig. 2 | QD charging and neutral exciton linewidth.
a, Measured photoluminescence signal of non-resonantly excited QD4
($\lambda = 830$ nm, $P = 200$ nW, $B = 0.00$ T) as a function of gate voltage. The three main
charge states of the QD are the positive trion (X^+), neutral exciton (X^0) and
negative trion (X^-). Dark blue, maximum number of counts; white, minimum
number of counts. **b**, Resonance fluorescence on QD5 (X^0, $\lambda = 939$ nm,
$B = 0.00$ T) excited well below saturation (red solid line, Lorentzian fit). From
the measured Stark shift of 240 GHz V^{-1}, a linewidth of 0.32 GHz is obtained,
which is close to the typical transform limit of 0.25 GHz for these InGaAs QDs at
a wavelength of 940 nm (ref. [39]). The splitting arises from the fine structure of
X^0 and is 11.05 GHz for QD5.
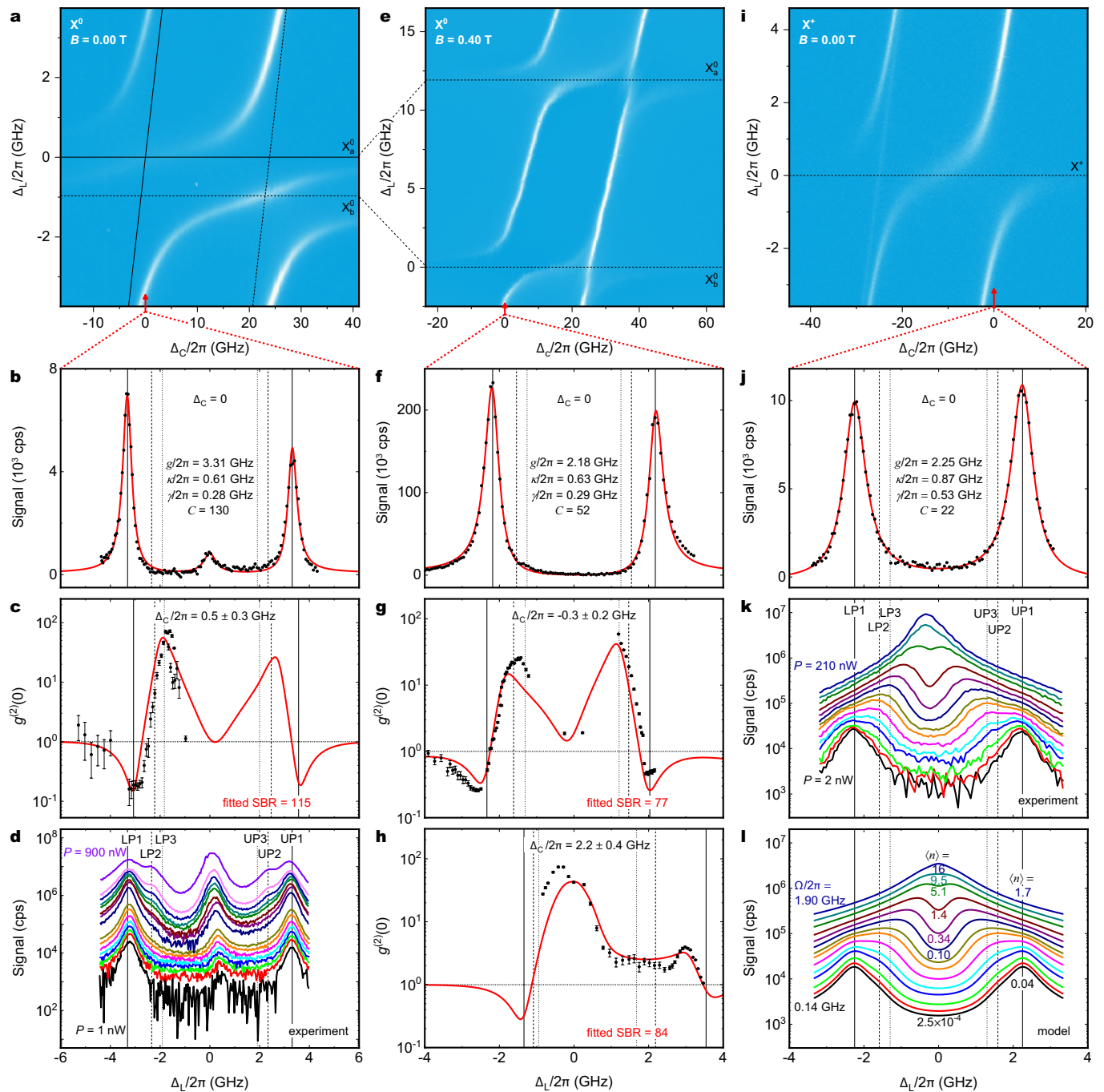
Extended Data Fig. 3 | Spectroscopy on cavity-coupled QD1. a, X^0 at $B = 0.00$ T. RF scan revealing two transverse-electromagnetic (TEM$_{00}$) cavity modes with a polarization splitting of 25 GHz (inclined lines) coupled to two FSS levels of X^0 with a splitting of 1 GHz (horizontal lines). **b**, Line cut at resonance with the 'left' cavity mode (as indicated by red arrow). The main peaks arise from coupling of the 'high'-frequency X^0 transition to one cavity mode; the peak at $\Delta_L = 0$ arises from coupling of the 'low'-frequency X^0 transition to the same cavity mode. **c**, $g^{(2)}(0)$ versus laser detuning for a cavity detuning close to zero. **d**, Power dependence at resonance. Excitation of the second rung of the Jaynes–Cummings ladder (LP2, UP2) is evident at high powers, as indicated by the dashed vertical lines. **e**, X^0 at $B = 0.40$ T. RF scan revealing that the same TEM$_{00}$ cavity modes couple to the two X^0 transitions. The X^0 transitions are now separated by Zeeman splitting. **f**, Line cut at resonance with the 'left' cavity mode. **g**, **h**, $g^{(2)}(0)$ versus laser detuning for two

different cavity detunings: one close to zero and one close to g. **i**, X^+ at $B = 0.00$ T. RF scan of the X^+ transition. **j**, Line cut at resonance with the 'right' cavity mode. **k**, **l**, Experimental (**k**) and theoretical (**l**) power dependence at resonance. The excitation of higher rungs of the Jaynes–Cummings ladder is evident by the convergence from the two first-rung polaritons towards the bare-cavity mode with increasing power, leading to a calculated mean photon number in the cavity of up to $\langle n \rangle = 16$. The Hilbert space in the model is truncated to 35 rungs of the Jaynes–Cummings ladder. The slight frequency shift of the signal peak in **k** at maximum laser power is due to an unintended drift of the cavity length during this experiment. In all figures, the vertical lines depict the resonance frequencies for the first three rungs of the Jaynes–Cummings ladder (LP1, UP1: solid; LP2, UP2: dashed; LP3, UP3: dotted) at a particular cavity detuning. Error bars in **c**, **g**, **h** are one standard error.
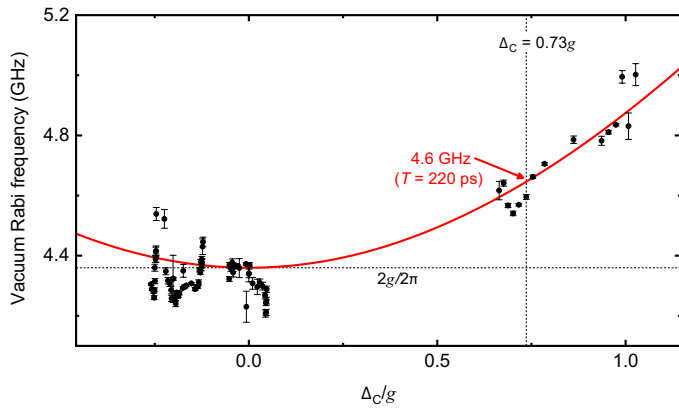
Extended Data Fig. 4 | Vacuum Rabi frequency versus Δ_C. The data points correspond to measured vacuum Rabi frequencies (determined via FFT of $g^{(2)}(\tau)$) for different cavity detunings Δ_C. The red solid line is the result of an analytical calculation of the polariton splitting in the $|1\pm\rangle$ manifold for different values of Δ_C (see equation (15) in Supplementary Information section III) using a coupling strength measured spectroscopically (Extended Data Fig. 3f). Error bars are one standard error. Data are from X^0 in QD1 at $B = 0.40$ T.
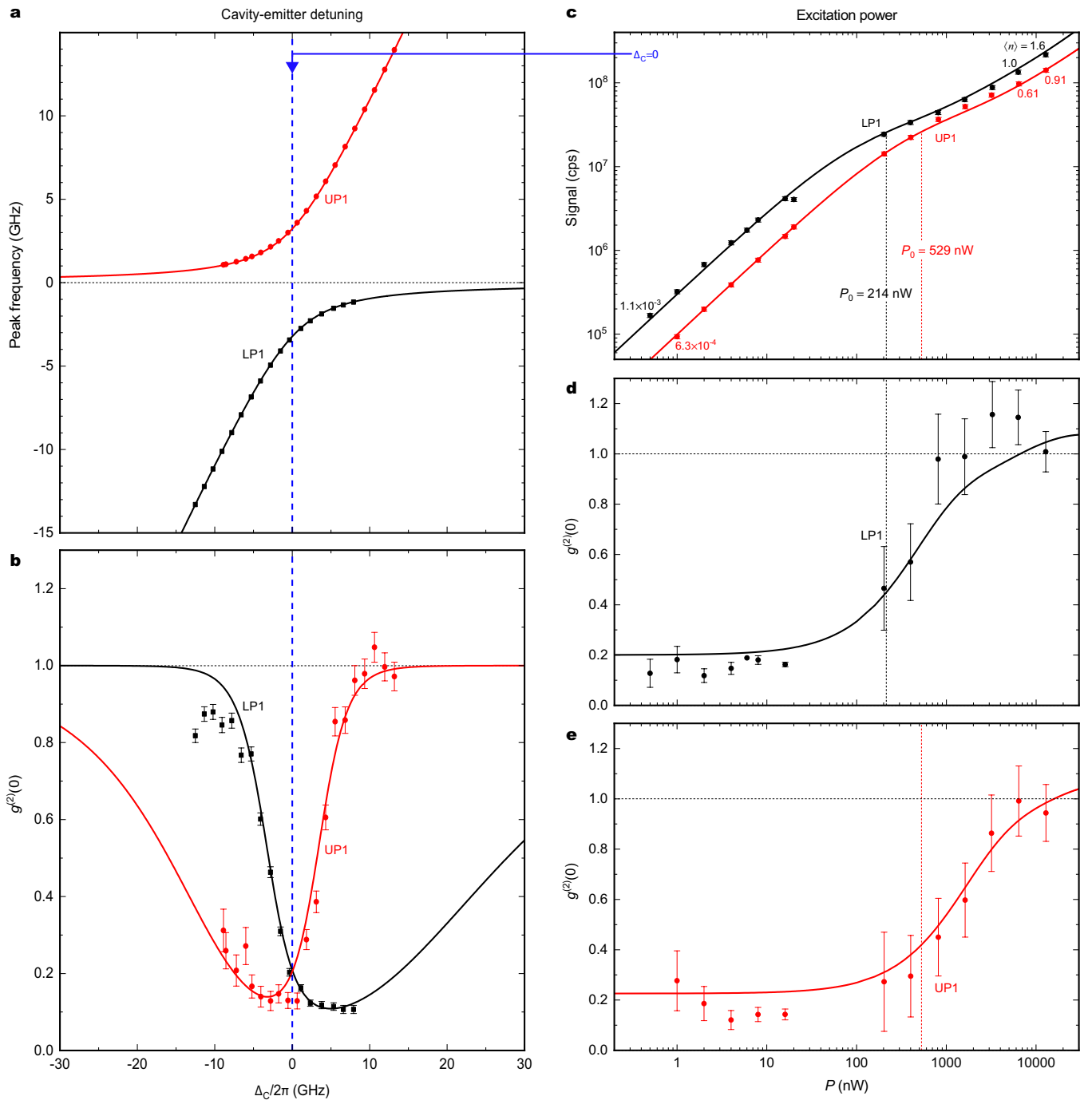
Extended Data Fig. 5 | Spectroscopy of cavity-coupled QD2. a, Experimental and theoretical dispersion of the lower (LP1) and the upper (UP1) polariton. **b**, Corresponding experimental and theoretical $g^{(2)}(0)$ values. **c**, Intensity of scattered light from LP1 and UP1 at zero cavity detuning as a function of resonance excitation power. The absence of saturation is due to the population of higher rungs of the Jaynes–Cummings ladder with increasing power. The behaviour at low powers allows the dependence of the Rabi frequency Ω on laser power P to be determined. This behaviour is parameterized with power P_0 (see text for definition): $P_0 = 214$ nW for LP1 and $P_0 = 529$ nW for UP1 (black and red dashed vertical lines, respectively). The mean photon number $\langle n \rangle$ is shown. **d**, **e**, Corresponding experimental and theoretical $g^{(2)}(0)$ values for LP1 (**d**) and UP1 (**e**). Error bars in **b**–**e** are one standard error. All data are from X^0 in QD2 at $B = 0.50$ T.